LA-UR-14-27919
Approved for public release; distribution is unlimited.

Title: Derivation of effective fission gas diffusivities in UO2 from lower length scale simulations and implementation of fission gas diffusion models in BISON

Author(s): Andersson, Anders David Ragnar
Pastore, Giovanni
Liu, Xiang-Yang
Perriot, Romain Thibault
Tonks, Michael
Stanek, Christopher Richard

Intended for: Report

Issued: 2014-11-07 (rev.1)

Derivation of effective fission gas diffusivities in UO_2 from lower length scale simulations and implementation of fission gas diffusion models in BISON

David A. Andersson,[1] Giovanni Pastore,[2] Xiang-Yang Liu,[1]
Romain Perriot,[1] Michael R. Tonks,[3] and Christopher R. Stanek[1]

[1] *Materials Science and Technology Division, Los Alamos National Laboratory, Los Alamos, NM 87545*
[2] *Fuel Modeling and Simulation, Idaho National Laboratory, P.O. Box 1625, Idaho Falls, ID 83415*
[3] *Fuel Modeling and Simulation Department, Idaho National Laboratory, P.O. Box 1625, Idaho Falls, ID 83415*

This report summarizes the development of new fission gas diffusion models from lower length scale simulations and assessment of these models in terms of annealing experiments and fission gas release simulations using the BISON fuel performance code. Based on the mechanisms established from density functional theory (DFT) and empirical potential calculations, continuum models for diffusion of xenon (Xe) in UO_2 were derived for both intrinsic conditions and under irradiation. The importance of the large Xe_{U_3O} cluster (a Xe atom in a uranium + oxygen vacancy trap site with two bound uranium vacancies) is emphasized, which is a consequence of its high mobility and stability. These models were implemented in the MARMOT phase field code, which is used to calculate effective Xe diffusivities for various irradiation conditions. The effective diffusivities were used in BISON to calculate fission gas release for a number of test cases. The results are assessed against experimental data and future directions for research are outlined based on the conclusions.

I. INTRODUCTION

In UO_2 nuclear fuel, the retention and release of fission gas atoms such as xenon (Xe) are important for nuclear fuel performance. For example, the formation of fission gas bubbles induces fuel swelling, which contributes to mechanical interaction with the clad thereby increasing the probability of clad breach. Fission gas bubbles also decrease the thermal conductivity of the fuel. Alternatively, fission gas can be released from the fuel to the plenum. This increases the pressure on the clad walls. In order to predict the fuel performance as function of burn-up, the redistribution of fission gas atoms must be understood[1]. Most fission gases have low solubility in the fuel matrix, which is especially pronounced for large fission gas atoms such as Xe. As a result there is a significant driving force for segregation of gas atoms to extended defects, e.g. grain boundaries and dislocations, and subsequently for nucleation of gas bubbles at these sinks. After segregating to grain boundaries fission gases may be released to the fuel plenum, either by fast diffusion of individual gas atoms along grain boundaries or by interlinked gas bubbles forming percolation networks.

Several empirical or semi-empirical models of fission gas retention and release in UO_2 nuclear fuel have been developed[2–9]. Most of these models rely on the analysis by Turnbull *et al.* for description of diffusion of atoms in bulk UO_2 (Stage 1 of fission gas release)[8,10–15]. Turnbull *et al.* divided the diffusivity into three temperature ranges[10–13,15]. At high temperature (D_1, $T > 1650$ K) intrinsic diffusion dominates and the diffusivity for stoichiometric UO_2 was taken from Davies and Long[16], who reported an activation energy of 3.04 eV (E_a) and a pre-exponential factor (D_0) of $7.6 \cdot 10^{-10}$ m^2/s,

$$D = D_0 \exp\left(-\frac{E_a}{k_B T}\right). \quad (1)$$

The uncertainty of the fission gas diffusion coefficient as function of, for example, temperature, was discussed in the review by Lawrence[17]. For example, at 1400°C they found diffusivities ranging many orders of magnitude between studies, which can be attributed to several experimental factors of which sample non-stoichiometry (x in $UO_{2\pm x}$) was identified as the most important[17]. The sample non-stoichiometry is controlled by temperature and the chemistry of the experimental setup, for example, whether the measurement was carried out in vacuum or in flowing H_2 gas, and the material used for the sample holder. Experimental data for the activation energies span values from 2.87 eV to 3.95 eV and pre-exponential factors from 5×10^{-4} m^2/s to 2.90×10^{-12} m^2/s[18–20]. Typically, a higher activation energy is compensated by a higher pre-exponential factor, which is expected since the stoichiometry is maintained close to UO_2 for all cases. The results due to Davies and Long[16] and Miekeley *et al.*[18] are plotted in Fig. 1. We report two data sets from Davies and Long[16], the first corresponds to the model used in the fission gas release simulations and the second to measurements on plasma fused samples annealed in vacuum at 1650°C (in addition to the sintering procedure used for the first sample set). Clearly, the two samples give different answers, however the explanation for this behavior has not been established.

In the intermediate temperature range (D_2, $1381 < T < 1650$ K), radiation-enhanced diffusion dominates over intrinsic diffusion. The activation energy was derived from a rate theory model of the concentration of radiation-induced vacancies (proportional to the square root of the fission rate, $\dot{F}$) and the assumption that the rate-limiting step for Xe transport is diffusion of uranium vacancies[12,13], which gives an activation energy of 1.20 eV and $D_0 = 4 \times 1.41 \cdot 10^{-25} \times \sqrt{\dot{F}}$ m^2/s. Below 1381 K (D_3), Xe diffusion is athermal and proportional to the fission rate[12–14]. The Turnbull model for irradiation

enhanced diffusion is also plotted in Fig. 1.

Although analysis of diffusivity data allows for determination of D_1, D_2 and D_3, there is still uncertainty regarding diffusion mechanisms as well as the detailed relation between diffusivities and the thermodynamic (i.e. non-stoichiometry) and irradiation conditions. We have previously performed studies using DFT and empirical potentials to investigate the underlying diffusion mechanisms[21]. Here we expand this work to include larger and fast moving Xe-vacancy clusters as well as complete coupling between different mechanisms by solving the corresponding system of reaction-diffusion equations in MARMOT.

In this report, we first derive diffusion models and parametrization from lower length-scale simulations (Sec. II). The results are described in Sec. III. We start by presenting the calculation of effective fission gas diffusivities (Sec. III A), followed by discussion of possible contribution to irradiation enhanced diffusion at intermediate and low temperature from fission gas bubbles (Sec. III B). The results are compared to post-irradiation annealing experiments. Next, the diffusion models are used in the BISON fuel performance code to simulate fission gas release in two Risø ramp tests (Sec. IV).

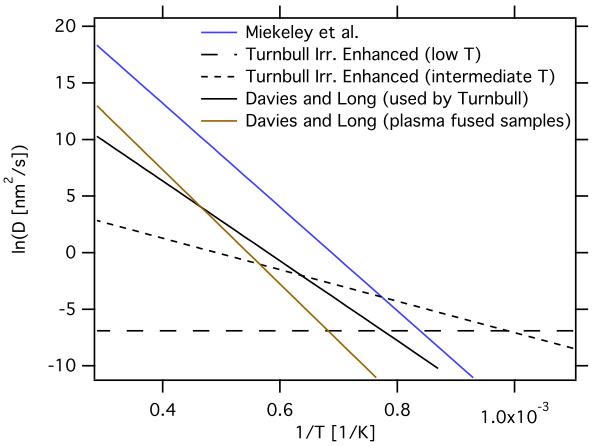

FIG. 1. The Xe diffusivity measured by Miekeley *et al.*[18], Davies and Long[16] and by Turnbull *et al.*[12]. The plot does not contain the raw experimental data, but rather the Arrhenius model derived from the experimental data.

II. XE, U VACANCY AND U INTERSTITIAL DIFFUSION MODELS

The Xe, U vacancy and U interstitial diffusion and reaction models were described in an earlier NEAMS report. Here we recapitulate the most important results and conclusions. We also expand the model to include the Xe_{U_3O} cluster, which was previously, as it seems incorrectly, assumed to have negligible impact on bulk diffusion. These models form the basis for the MARMOT and BISON simulations.

A. Model derivation

The redistribution of Xe, U vacancies and U interstitials may be described by diffusion equations:

$$\frac{\partial y_X}{\partial t} = \nabla \cdot (D_X \nabla y_X)\,, \tag{2}$$

where X denotes either Xe, U vacancies or U interstitials, y_X is the corresponding concentration (fractional) and D_X the effective diffusivity, which is a function of, e.g., the species concentration, irradiation conditions, microstructure and temperature. In order to accurately express the diffusivities as function of these parameters, we develop models that capture the mechanistic aspects of diffusion.

DFT and empirical potential calculations have shown that Xe atoms occupy U vacancy trap sites, which may also include oxygen vacancies depending on the $UO_{2\pm x}$ (non-)stoichiometry[21–24]. In this study we assume nearly stoichiometric UO_2, for which the preferred trap site is a U vacancy coordinated with one oxygen (O) vacancy (Xe_{UO})[21–24]. The charge state of this cluster (the number of bound holes) is also important and for stoichiometric UO_2 it is fully charged (no bound holes, Xe''_{UO} in modified Kröger-Vink notation)[21]. O defects or ions will not be explicitly treated in this study, because their dynamics are many orders of magnitude faster than for Xe atoms and U ions, which implies that the O defect concentration can be assumed to fulfill equilibrium conditions. The same conclusion applies to electronic defects. The Xe_{UO} cluster is not mobile due to the high migration barrier associated with cation exchange mechanisms, but diffusion rather occurs by binding another U vacancy to the trap site, which in stoichiometric UO_2 creates a cluster denoted Xe_{U_2O} (Xe occupying a trap site consisting of two U vacancies and one O vacancy, which is fully charged, Xe''''''_{U_2O} in Kröger-Vink notation). The contribution to diffusion from this cluster is governed by the intracluster vacancy migration barrier (the rate-limiting migration step), $G_M^{V_U^C}$, and the binding energy of vacancies to the Xe trap site (governing the concentration of these clusters), $G_B^{V_U}$.

Based on this mechanism, the Xe diffusivity is expressed as ($y_{Xe}^{TOT} = y_{Xe_{UO}} + y_{Xe_{U_2O}}$):

$$\frac{\partial y_{Xe}^{TOT}}{\partial t} = \frac{\partial y_{Xe_{U_2O}}}{\partial t} = \\ = \nabla \cdot \left(M_{Xe_{U_2O}} y_{Xe_{U_2O}} \nabla \left(\mu_{Xe_{U_2O}} - 2\mu_U - \mu_O\right)\right), \tag{3}$$

where $M_{Xe_{U_2O}}$ is the mobility of the Xe_{U_2O} cluster, $y_{Xe_{U_2O}}$ is the cluster concentration, $\mu_{Xe_{U_2O}} - 2\mu_U - \mu_O$ is the diffusion potential for the above mechanism (μ_X is the chemical potential of each species) and $-\frac{M_{Xe_{U_2O}} y_{Xe_{U_2O}}}{V_m} \nabla \left(\mu_{Xe_{U_2O}} - 2\mu_U - \mu_O\right)$ is the flux ($J_{Xe_{U_2O}}$). V_m is the molar volume. The mobility (M) is related to the diffusivity (D) by $M = \frac{D}{k_B T}$. The chemical potential gradients are used in order to be consistent

with phase field models. The right hand side of Eq. 3 simplifies to the regular diffusion equation if the Xe_{U_2O} cluster in UO_2 behaves as an ideal solution. Xe atoms in trap sites without a bound U vacancy (Xe_{UO}) are immobile and thus do not contribute to diffusion and do not appear in Eq. 3. Also, the oxygen chemical potential, μ_O, disappears when the gradient is applied since it is assumed to fulfill equilibrium conditions ($\nabla\mu_O = 0$). Finally, the cluster reaction rate equations derived below will eventually be included in the time evolution for each cluster, which means that Eq. 3 should not be viewed as complete (see below for details).

The mobile Xe_{U_2O} cluster treated above may bind another vacancy to form a Xe_{U_3O} cluster. Again, the charge state of this cluster (the number of bound holes) is important and for stoichiometric UO_2 we assume the cluster to be fully charged (no bound holes, Xe_{U_3O}'''''''' in modified Kröger-Vink notation)[21]. Due to the high charge of this cluster we also investigate the sensitivity of our conclusions to the charge state, in particular its effect on the cluster binding energy. As for the Xe_{U_2O} cluster, the contribution to diffusion from the Xe_{U_3O} cluster is governed by the intracluster vacancy migration barrier (the rate-limiting migration step), $G_M^{V_{U_2}^C}$, and the binding energy of an additional vacancy to the Xe_{U_2O} cluster (governing the concentration of these clusters), $G_B^{V_{U_2}}$. When both the Xe_{U_2O} and Xe_{U_3O} clusters are included, the Xe diffusivity is expressed as ($y_{Xe}^{TOT} = y_{Xe_{UO}} + y_{Xe_{U_2O}} + y_{Xe_{U_3O}}$):

$$\begin{aligned}\frac{\partial y_{Xe}^{TOT}}{\partial t} = \frac{\partial y_{Xe_{U_2O}}}{\partial t} + \frac{\partial y_{Xe_{U_3O}}}{\partial t} = \\ = \nabla\cdot\left(M_{Xe_{U_2O}} y_{Xe_{U_2O}} \nabla\left(\mu_{Xe_{U_2O}} - 2\mu_U - \mu_O\right)\right) + \\ + \nabla\cdot\left(M_{Xe_{U_3O}} y_{Xe_{U_3O}} \nabla\left(\mu_{Xe_{U_3O}} - 3\mu_U - \mu_O\right)\right),\end{aligned} \tag{4}$$

where $M_{Xe_{U_3O}}$ is the mobility of the Xe_{U_3O} cluster, $y_{Xe_{U_3O}}$ is the cluster concentration, $\mu_{Xe_{U_3O}} - 3\mu_U - \mu_O$ is the diffusion potential for the above mechanism and $-\frac{M_{Xe_{U_3O}} y_{Xe_{U_3O}}}{V_m}\nabla\left(\mu_{Xe_{U_3O}} - 3\mu_U - \mu_O\right)$ is the flux ($J_{Xe_{U_3O}}$). V_m is the molar volume. Other parameters are the same as in Eq. 3 and the interoperation of each parameter also follows the discussion for this equation. The oxygen chemical potential, μ_O, disappears when the gradient is applied, since it is assumed to fulfill equilibrium conditions ($\nabla\mu_O = 0$).

Diffusion of uranium via vacancy mechanisms has also been investigated by DFT calculations. For the high vacancy concentrations that may occur under irradiation, these calculations emphasize the importance of vacancy clustering (U divacancies, V_{U_2}) due to attractive vacancy binding energy and the much higher mobility of clusters compared to single vacancies. Both single vacancies and divacancies are fully charged in nearly stoichiometric UO_2, i.e. in Kröger-Vink notation the defects are V_U'''' and V_{U_2}''''''''. The diffusion of vacancies and divacancy clusters is described by:

$$\frac{\partial y_{V_U}}{\partial t} = \nabla\cdot\left(M_{V_U} y_{V_U} \nabla\left(\mu_{V_U} - \mu_U\right)\right) \tag{5}$$

and

$$\frac{\partial y_{V_{U_2}}}{\partial t} = \nabla\cdot\left(M_{V_{U_2}} y_{V_{U_2}} \nabla\left(\mu_{V_{U_2}} - 2\mu_U\right)\right), \tag{6}$$

where M_{V_U} and $M_{V_{U_2}}$ are the vacancy mobilities and $(\mu_{V_U} - \mu_U)$ and $\left(\mu_{V_{U_2}} - 2\mu_U\right)$ the corresponding diffusion potentials giving rise to the fluxes $-\frac{M_{V_U} y_{V_U}}{V_m}\nabla\left(\mu_{V_U} - \mu_U\right)$ and $-\frac{M_{V_{U_2}} y_{V_{U_2}}}{V_m}\nabla\left(\mu_{V_{U_2}} - 2\mu_U\right)$. The time evolution of the total vacancy concentration ($y_{Va}^{TOT} = y_{V_U} + 2y_{V_{U_2}}$) is expressed as the sum of these two contributions. The interoperation of these parameters follows the discussion for Eq. 3.

Finally, diffusion of U interstitials is described by:

$$\frac{\partial y_{U_I}}{\partial t} = \nabla\cdot\left(M_{U_I} y_{U_I} \nabla\left(\mu_{U_I} - \mu_{V_I}\right)\right), \tag{7}$$

where M_{U_I} is the mobility of interstitials and $(\mu_{U_I} - \mu_{V_I})$ is the diffusion potential for interstitials (V_I denotes empty interstitial sites), which results in a flux equal to $-\frac{M_{U_I} y_{U_I}}{V_m}\nabla\left(\mu_{U_I} - \mu_{V_I}\right)$.

Eqs. 3, 4, 5, 6 and 7 contain five or six (depending on whether the Xe_{U_3O} cluster is included or not) independent concentration variables; $y_{Xe_{UO}}$ (concentration of Xe in vacancy trap sites), y_{V_U} (concentration of U vacancies), $y_{Xe_{U_2O}}$ (concentration of Xe trap sites with a bound vacancy), $y_{Xe_{U_3O}}$ (concentration of Xe trap sites with two bound vacancies), $y_{V_{U_2}}$ (concentration of uranium divacancies) and y_{U_I} (concentration of U interstitials). The concentrations of U ions on the cation sublattice and vacancies on the interstitial sublattice are dependent variables given by site conservation. In addition to the diffusion equations above, these five or six variables are coupled by cluster formation and recombination reactions. Vacancies and interstitials are created and annihilated at sources and sinks, such as dislocations, grain boundaries and voids or gas bubbles. However, under irradiation, cascade events are the major source of vacancies and interstitials. All of these reactions may be captured by reaction rate equations, which, unlike the diffusion equations, do not involve any gradients. Because we are interested in diffusion under irradiation, it is not sufficient to apply equilibrium conditions for the defect concentrations. In our model the formation of Xe_{U_2O} clusters occurs according to the following reaction:

$$Xe_{UO} + V_U \rightleftharpoons Xe_{U_2O}. \tag{8}$$

The corresponding reaction rate is expressed as (Reaction 8):

$$\begin{aligned}\frac{\partial y_{Xe_{U_2O}}}{\partial t} = y_{Xe_{UO}} y_{V_U} \frac{M_{V_U}}{S^2} \times \\ Z\left(\mu_{Xe_{U_2O}} - \mu_{Xe_{UO}} - \mu_{V_U}\right),\end{aligned} \tag{9}$$

where S is the atomic jump distance for the defects, Z is the number of sites from which reaction between, e.g., Xe_{UO} and V_U, is inevitable (related to the reaction radius) and the difference in chemical potential represents

the driving force for the reaction. Note that if the driving force is negative, the rate changes sign and thus the net direction of the reaction. Eq. 8 is equivalent to a typical rate theory equation using the equilibrium concentration of defects to express the driving force and the diffusivity for the rate constant. We use the form in Eq. 9 to be consistent with phase field models, which applies to all reaction rate equations below. Note that the mobility of Xe in the vacancy trap site ($M_{Xe_{UO}}$) is zero, and it is thus not included in Eq. 9. In the general case the mobility factor in this equation is the sum of the mobility of the individual defects, $\frac{M_{Xe_{UO}}}{S^2} + \frac{M_{V_U}}{S^2}$, which simplifies to $\approx \frac{M_{V_U}}{S^2}$ for this special case. The driving force in Eq. 9, as well as the forces in the other reaction rate theory equations below, are formulated such that thermodynamic equilibrium is attained at steady state, $\frac{\partial y_X}{\partial t} = 0$ and it is thus consistent with the standard way of expressing rate theory equations. U interstitials may annihilate with Xe_{U_2O} clusters to form a single Xe atom in a trap site without a bound vacancy ($Xe_{U_2O} + U_I \rightleftharpoons Xe_{UO} + V_I + U_U$), the rate of which is given by:

$$\frac{\partial y_{Xe_{U_2O}}}{\partial t} = -y_{Xe_{U_2O}} y_{U_I} \left(\frac{M_{Xe_{U_2O}}}{S^2} + \frac{M_{U_I}}{S^2} \right) \times Z \left(\mu_{Xe_{U_2O}} + \mu_{U_I} - \mu_{Xe_{UO}} - \mu_{V_I} - \mu_{U_U} \right). \tag{10}$$

The total Xe_{U_2O} reaction rate is obtained as the sum of Eqs. 9 and 10.

The formation of the Xe_{U_3O} cluster involves two reactions:

$$Xe_{U_2O} + V_U \rightleftharpoons Xe_{U_3O} \tag{11}$$

and

$$Xe_{UO} + V_{U_2} \rightleftharpoons Xe_{U_3O}. \tag{12}$$

The reaction rates are formulated as:

$$\frac{\partial y_{Xe_{U_3O}}}{\partial t} = y_{Xe_{U_2O}} y_{V_U} \left(\frac{M_{V_U}}{S^2} + \frac{M_{Xe_{UO}}}{S^2} \right) \times Z \left(\mu_{Xe_{U_3O}} - \mu_{Xe_{U_2O}} - \mu_{V_U} \right) \tag{13}$$

and

$$\frac{\partial y_{Xe_{U_3O}}}{\partial t} = y_{Xe_{UO}} y_{V_{U_2}} \frac{M_{V_{U_2}}}{S^2} \times Z \left(\mu_{Xe_{U_3O}} - \mu_{Xe_{UO}} - \mu_{V_{U_2}} \right). \tag{14}$$

U interstitials may annihilate with Xe_{U_3O} clusters to form Xe_{U_2O} clusters ($Xe_{U_3O} + U_I \rightleftharpoons Xe_{U_2O} + V_I + U_U$), the rate of which is given by:

$$\frac{\partial y_{Xe_{U_3O}}}{\partial t} = -y_{Xe_{U_3O}} y_{U_I} \left(\frac{M_{Xe_{U_3O}}}{S^2} + \frac{M_{U_I}}{S^2} \right) \times Z \left(\mu_{Xe_{U_3O}} + \mu_{U_I} - \mu_{Xe_{U_2O}} - \mu_{V_I} - \mu_{U_U} \right). \tag{15}$$

The total Xe_{U_3O} reaction rate is obtained as the sum of Eqs. 13, 14 and 15.

The formation of U vacancy clusters (V_{U_2}),

$$V_U + V_U \rightleftharpoons V_{U_2}, \tag{16}$$

occurs with the following rate

$$\frac{\partial y_{V_{U_2}}}{\partial t} = y_{V_U} y_{V_U} \frac{2M_{V_U}}{S^2} Z \left(\mu_{V_{U_2}} - 2\mu_{V_U} \right). \tag{17}$$

The vacancy clusters may be annihilated by U interstitials ($V_{U_2} + U_I \rightleftharpoons V_U + V_I + U_U$) and at sinks according to the following rate:

$$\frac{\partial y_{V_2}}{\partial t} = K_{V_2} - y_{V_2} y_{U_I} \left(\frac{M_{V_2}}{S^2} + \frac{M_{U_I}}{S^2} \right) \times Z(\mu_{V_2} + \mu_{U_I} - \mu_{Va} - \mu_{V_I} - \mu_{U_U}) - M_{V_2} k_B T y_{V_2} k_{V_2}^2, \tag{18}$$

which also include a source term due to cascade events ($K_{V_{U_2}}$). In Eq. 18, k_B is the Boltzmann constant and $k_{V_{U_2}}^2$ is the strength of fixed vacancy sinks. As for the Xe_{U_2O} clusters, the total V_{U_2} reaction rate is obtained as the sum of Eqs. 17 and 18.

The formation rate of vacancies (K_{V_U}) and interstitials ($K_{U_I} = K_{V_U} + 2K_{V_{U_2}}$) is determined by the irradiation conditions. Vacancies and interstitials may be annihilated by mutual recombination or by reactions with fixed sinks such as voids, fission gas bubbles, grain boundaries and dislocations. The interstitial and vacancy sink strengths are labeled $k_{U_I}^2$ and $k_{V_U}^2$, respectively. This gives the following reaction rate equations:

$$\frac{\partial y_{V_U}}{\partial t} = K_{V_U} - M_{V_U} k_B T y_{V_U} k_{V_U}^2 - \left(\frac{M_{V_U}}{S^2} + \frac{M_{U_I}}{S^2} \right) \times Z y_{V_U} y_{U_I} \left(\mu_{V_U} + \mu_{U_I} - \mu_{V_I} - \mu_{U_U} \right) \tag{19}$$

and

$$\frac{\partial y_{U_I}}{\partial t} = K_{U_I} - M_{U_I} y_{U_I} k_{U_I}^2 - \left(\frac{M_{V_U}}{S^2} + \frac{M_{U_I}}{S^2} \right) \times Z y_{V_U} y_{U_I} \left(\mu_{V_U} + \mu_{U_I} - \mu_{V_I} - \mu_{U_U} \right). \tag{20}$$

The total V_U reaction rate is obtained as the sum of Eq. 19, the negative of Eq. 17, Eq. 9 and Eq. 13 as well as the interstitial term of Eq. 18. Similarly, the total interstitial reaction rate is given by the sum of Eqs. 20, 10, 15 and the interstitial term of Eq. 18.

Other reactions and clusters are possible. However, further growth of the clusters is similar to bubble nucleation, which is treated separate from Xe bulk diffusion in fission gas release models. These aspects will be explored in future work. We will discuss the possibility of fission gas bubble diffusion being responsible for increased diffusion rates at low temperature in Sec. III B. However, additional work is required to solidify this connection.

B. Model parameters

Most of the parameters in Eqs. 3, 4, 5, 6, 7, 9, 10, 17, 18, 19 and 20 have been calculated using DFT and empirical potentials[21]. The defect mobilities are listed in Table I. In order to obtain the chemical potentials and the differences in chemical potentials defining the driving forces, we first need to express the total free energy of the $(U_U, V_U, V_{U_2}, Xe_{UO}, Xe_{U_2O})(V_I, U_I)O_2$ system (see below for discussion about adding the Xe_{U_3O} cluster to this model), where the parentheses separate different sublattices and the symbols indicate the defect types that are contained on each sublattice. Xe atoms are assumed to exclusively occupy vacancy trap sites, i.e. the concentration of interstitial Xe atoms is negligible. By applying a quinary regular solution model for the cation sublattice and an ideal solution model for the interstitial sublattice as well as the gradient energy terms required to describe dissolution kinetics, the following free energy density functional is obtained:

$$\frac{G_m^{Total}(y_s,T)}{N_A} = \sum_s y_s {}^oG_s^{UO_2} + \sum_s k_B T\left(y_s \ln\left(y_s\right)\right) + \\ + \sum_{s_1,s_2,s_1\neq s_2} {}^0L_{s_1,s_2} y_{s_1} y_{s_2} + \sum_s \frac{\epsilon_s}{2}\left(\nabla y_s\right)^2. \quad (21)$$

Here s covers all species on the cation and interstitial sublattices (U_U, Xe_{UO}, Xe_{U_2O}, V_U, V_{U_2}, U_I and V_{U_I}), y_s are the site fractions and ϵ_s the gradient energy of species s. ${}^0L_{s_1,s_2}$ are the regular solution parameters for interaction between species s_1 and s_2 on the cation sublattice (s_1 and s_2 are U_U, Xe_{UO}, Xe_{U_2O}, V_U and V_{U_2}). N_A is Avogadro's number converting the left hand side of the equation to energy per atom rather than mole (this convention will be applied throughout this work). Site conservation implies that:

$$y_{U_U} + y_{Xe_{UO}} + 2y_{Xe_{U_2O}} + y_{V_U} + 2y_{V_{U_2}} = 1 \quad (22)$$

and

$$y_{U_I} + y_{V_I} = 1. \quad (23)$$

The ${}^oG_s^{UO_2} = {}^oH_s^{UO_2} - T{}^oS_s^{UO_2}$ terms were defined according to the defect formation (V_U, V_{U_2}, U_I) or solution (Xe_{UO} and Xe_{U_2O}) energies and entropies combined with cluster binding energies and entropies, as calculated from DFT and empirical potentials (see Table I[21]). These parameters are all functions of the $UO_{2\pm x}$ non-stoichiometry[21]. The data in Table I assumes nearly stoichiometric UO_2, but can easily be extended to other non-stoichiometries based on data presented in, e.g., Ref. 21. The Xe reference state is defined as the gas phase at 298 K and 100000 Pa. The ${}^oG_U^{UO_2}$ reference is set to 0 eV. The ${}^oG_s^{UO_2}$ parameters are constants and thus only relevant for the reaction rate equations ($\nabla {}^oG_s^{UO_2} = 0$ in the diffusion equations). The regular solution parameters ${}^0L_{s_1,s_2}$ were calculated from the DFT binding energies (E_B) and the number of available binding sites (Z_B):

$${}^0L_{s_1,s_2} = \frac{Z_B}{2} E_B. \quad (24)$$

Only the most stable site for each defect was considered. The temperature dependence of the regular solution parameters (${}^0L_{s_1,s_2} = {}^0L^0_{s_1,s_2} + {}^0L^1_{s_1,s_2}T$) was set to zero (${}^0L^1_{s_1,s_2} = 0$ eV). The ${}^0L_{s_1,s_2}$ values are summarized in Table I. The values reflect the strong binding between Xe atoms and vacancies as well as that between Xe atoms themselves, which capture the tendency to nucleate fission gas bubbles. However, the present model is not optimized to capture the properties of bubbles, which is primarily a consequence of only treating U vacancies and not the O vacancies or bound Schottky defects (one U vacancy and two O vacancies) required to capture growth of bubbles. This topic is left as future work. We did not attempt to calculate the interfacial energies (ϵ_s) from either DFT or empirical potentials. Careful determination of these parameters is also left as future work. The chemical potential differences in the diffusion and reaction rate equations are calculated from the free energy density in Eq. 21 according to:

$$\mu_A - \mu_B = \frac{\delta}{\delta y_A}\left(\int_\Omega G_m^{Total} d\Omega\right)_{y_B} = \\ = \left(\frac{\partial G_m^{Total}}{\partial y_A}\right)_{y_B} - \nabla \cdot \left(\frac{\partial G_m^{Total}}{\partial \nabla y_A}\right)_{y_B}, \quad (25)$$

where B is treated as the dependent variable and Ω is the integration volume.

The model that includes the large Xe_{U_3O} cluster was formulated by adding 13, 14 and 15 as well as the corresponding diffusion equation (Eq. 4) to the Xe_{U_2O} reaction diffusion model presented above. The Xe_{U_3O} cluster must consequently be added to the free energy expression (Eq. 21) as well as to the site conservation expression (Eq. 22). In order to simplify the model implementation the Xe_{U_3O} cluster was treated as an ideal constituent, which implies that all interaction parameters involving these two clusters were set to zero, which is motivated by the small cluster concentrations. The formation energies entering the reaction rate equations and cluster diffusivities are listed in Table I and obtained from DFT calculations according to the same methodology as for the smaller clusters. Because calculated values were not available, the entropies were approximated as zero.

The remaining parameters K_{V_U}, $K_{V_{U_2}}$, K_{U_I}, $k^2_{V_U}$, $k^2_{V_2}$ and $k^2_{U_I}$ were estimated from experimental data[11,21] or treated as free parameters. Typical values are listed in Table I.

C. Numerical simulations

The diffusion and reaction rate equations (Eqs. 3, 4, 5, 6, 7, 9, 10, 17, 18, 19, 20, 13, 14 and 15 were implemented

Formation energies	${}^{o}H_s^{UO_2}$ (eV)	${}^{o}S_s^{UO_2}$ (k_B)
${}^{o}G_{U_U}^{UO_2}$	0.00	0.00
${}^{o}G_{V_U}^{UO_2}$	-0.19	-16.35
${}^{o}G_{V_{U_2}}^{UO_2}$	-0.30	7.19
${}^{o}G_{Xe_{UO}}^{UO_2}$	x	y
${}^{o}G_{Xe_{U_2O}}^{UO_2}$	$x-1.82$	$y+1.97$
${}^{o}G_{Xe_{U_3O}}^{UO_2}$	$x-5.09$	$y+1.97$
${}^{o}G_{V_I}^{UO_2}$	0.00	0.00
${}^{o}G_{U_I}^{UO_2}$	13.20	0.00
Regular solution parameters	${}^{0}L_{s_1,s_2}^{0}$ (eV)	${}^{0}L_{s_1,s_2}^{1}$ (k_B)
${}^{0}L_{Xe_{UO},V_U}$ (eV)	-10.92	0.00
${}^{0}L_{U_U,V_U}$ (eV)	1.80	0.00
${}^{0}L_{Xe_{UO},U_U}$ (eV)	9.12	0.00
${}^{0}L_{Xe_{U_2O},U_U}$ (eV)	5.04	0.00
${}^{0}L_{Xe_{U_2O},V_U}$ (eV)	-6.55	0.00
${}^{0}L_{Xe_{U_2O},Xe_{UO}}$ (eV)	-7.73	0.00
${}^{0}L_{Xe_{UO},V_{U_2}}$ (eV)	-9.51	0.00
${}^{0}L_{Xe_{U_2O}},V_{U_2}$ (eV)	16.49	0.00
${}^{0}L_{U_U,V_{U_2}}$ (eV)	4.80	0.00
${}^{0}L_{V_U,V_{U_2}}$ (eV)	-3.34	0.00
Kinetic parameters	D_0 (nm^2/s)	E_m (eV)
$D_{Xe_{U_2O}}$	$1.481\cdot10^{13}$	4.94
$D_{Xe_{U_3O}}$	$1.481\cdot10^{13}$	3.71
D_{V_U}	$7.121\cdot10^{11}$	4.72
$D_{V_{U_2}}$	$5.446\cdot10^{13}$	2.84
D_{U_I}	$1.2\cdot10^{12}$	4.70
Other parameters		
Z	1.0	
K (defects/U atom s)	$4.05\cdot10^{-6}$	
k_I^2 (1/nm^2)	0.012564	
k_V^2 (1/nm^2)	0.012564	

TABLE I. Bulk thermodynamic and kinetic parameters for defects in UO_2.

in the MARMOT phase field code[25], which is based on the MOOSE finite element framework[26,27]. The simulations used adaptive time-stepping. In order to avoid numerical instabilities for very low concentrations, logarithm terms and their derivatives were Taylor expanded below a certain threshold value (10^{-12}). The MARMOT simulations were used to calculate effective diffusivities, which were then used in BISON to simulate fission gas release.

III. RESULTS AND DISCUSSION

A. Simulations of effective Xe diffusivities in UO_2

The Xe diffusivity is a function of the vacancy concentration, which in thermodynamic equilibrium is expressed in terms of the vacancy formation energy. Ref. 21 performed this analysis for UO_2 based on the same data from DFT and empirical potentials as applied in our study (see Table I). They predicted an activation energy of 2.93 eV and a pre-exponential factor of $8.32\cdot10^{-12}$ m^2/s for Xe diffusion in stoichioemetric UO_2. Effective diffusivities may be calculated from our model by imposing flux boundary conditions at the left and right ends of a rectangular simulation cell and zero flux conditions at the top and bottom. The first set of simulations do not include the Xe_{U_3O} cluster. By measuring the steady state concentration gradient, the effective diffusivity is obtained as:

$$D_X = -\frac{J_X}{\nabla y_X} \tag{26}$$

By performing simulations at a number of different temperatures, the activation energy and pre-exponential factor, $D_X = D_0 \exp\left(-\frac{E_a}{k_B T}\right)$, can be extracted. The results are plotted in Fig. 2 and both $D_{Xe}^0 = 8.71\cdot10^{-12}$ and $E_a = 2.94$ eV agree well with the analytical results from Ref. 21. At the lower end of the temperature range, cluster formation starts to become controlling and the diffusivity tends towards that predicted for the mobile Xe trap site (Xe_{U_2O}). In this range diffusion is no longer limited by the vacancy concentration, i.e. the vast majority of Xe atoms exist as Xe_{U_2O} and the concentration of Xe_{UO} defects is negligible.

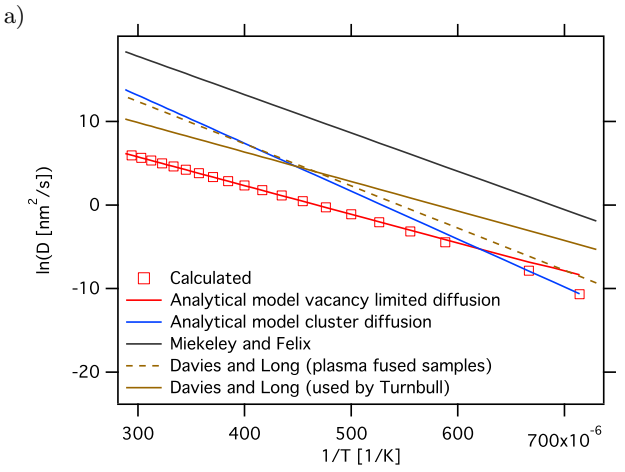

FIG. 2. The Xe diffusivity as function of temperature under intrinsic conditions calculated from MARMOT simulations. Models derived from the experimental data from Miekeley *et al.*[18] and Davies and Long (two data sets obtained from measurements on different samples)[16] are also shown.

In the next step we perform the same type of simula-

tion, but introduce damage via the K_{V_U}, $K_{V_{U_2}}$ and $K_{V_{U_I}}$ parameters (see K in Table I). Fig. 3a) plots the Xe diffusivity as function of temperature for a particular value of the damage rate ($4.05 \cdot 10^{-6}$ defects/U atom s). Fig. 3a) shows that at high and low temperature the predicted diffusivities approach the intrinsic values, while in the intermediate temperature regime, the damage gives rise to irradiation enhanced diffusion. The analytical models capture the diffusivity outside of the intermediate temperature range, but within this range the calculated diffusivity exceeds the analytical prediction from both the intrinsic and irradiation enhanced models. Compared to Turnbull's[12,13] model derived from experiments, our model underestimates the diffusivity across the full temperature range, see Fig. 3a). The discrepancy is especially noteworthy at low temperature where Turnbull[12,13] invokes irradiation enhanced vacancy concentrations as responsible for increased diffusion rates. The magnitude of this effect is clearly not supported by our model.

Fig. 3b) plots the effective diffusivity obtained when the Xe_{U_3O} cluster is included in the simulations. The driving force for diffusion is set to be the same for each mobile Xe cluster, which is achieved by adjusting the flux based on the mobility and concentration of each cluster. The damage rate and sink strengths are the same as in previous simulations (see Table I). Even though the concentration of Xe_{U_3O} clusters is small, its high mobility compared to Xe_{U_2O} gives a significant contribution to the diffusivity across almost the full temperature range. At the highest temperature in our simulations the diffusivity approaches the result when only the Xe_{U_2O} cluster is included, which also corresponds to the intrinsic result for the Xe_{U_2O} model. Below the highest temperatures the diffusivity is controlled by cluster diffusion. There is a balance between the Xe_{U_2O} and Xe_{U_3O} clusters, which implies that the effective diffusivity lies between these two limiting cluster diffusivities. This behavior extrapolates to low temperature. In the transition between the very high temperature behavior and the lower or intermediate temperature regime there is a switch from the Xe_{U_2O} cluster limited by the vacancy concentration (very high temperature) to a combination of the Xe_{U_2O} and Xe_{U_3O} clusters at lower temperatures. This gives rise to small temperature range with increasing diffusivity as temperature decreases. The diffusivity for the Xe_{U_3O} model in the intermediate temperature range agrees quite well with Turnbull's model[12,13], which is based on the diffusivity data from Davies and Long[16]. Note that the relevant range for this model is from just above 2000 K to about 1400-1500 K, where the agreement between the theoretical model and experiments is quite good. Davies and Long[16] found a range of diffusivities for different samples and our model agrees best with the results for plasma fused samples[16], in particular for the activation energy (slope of the diffusivity curves). The magnitude of the diffusivity is similar between the different samples investigated by Davies and Long[16]. However, while our simulations refer to in-pile conditions, the experiments by Davies and Long[16] were out-of-pile post-irradiation release experiments for which intrinsic conditions are typically assumed to be prevalent. Our results indicate that the effect of irradiation cannot always be ignored in the post-irradiation annealing experiments, which is further discussed in the next paragraph. At low temperature the diffusivity is still underestimated compared to the irradiation induced model proposed by Turnbull[12,13].

We have also performed simulations for the Xe_{U_3O} model without irradiation, see Figure 3b). Surprisingly the diffusivity increases rather than decreases with respect to the simulations with active defect production due to irradiation. This is contrary to our intuition and it is explained by the concentration of Xe_{U_3O} clusters increasing due to decreased recombination with uranium interstitial (U_I) defects. Under intrinsic conditions the interstitial concentration is very small, essentially negligible. At very high temperature the results again agree with the Xe_{U_2O} model, but in the intermediate range the diffusivity now exceeds that in Turnbull's[12,13] model based on the Davies and Long[16] data. Interestingly, the diffusivity agrees very well with the data reported by Miekeley *et al*[18]. This correlates with Miekeley *et al.*[18] samples being exposed to orders of magnitude smaller irradiation dose than the dose in the experiments by Davies and Long[16], which presumably correlates with the concentration of interstitials available for recombination with Xe_{U_3O} clusters in the diffusion anneal experiments, even though the quantitative relation remains to be worked out. This implies that the Xe_{U_3O} cluster contributes significantly to diffusion of Xe in nearly stoichiometric UO_2 due to a combination of its high stability and high mobility. The contribution from this cluster is higher for intrinsic conditions than under irradiation, which helps to explain some of the discrepancies between different experimental measurements, see Fig. 3b). In fact, the decrease in Xe diffusivity with increased irradiation has been observed in existing studies[28], but has traditionally been attributed to increased trapping. Additional work is required before we can draw solid conclusions regarding the relative importance of trapping and decreased concentration of mobile clusters due to interstitial recombination. Regardless, the Xe_{U_3O} model cannot explain the increased irradiation induced diffusivity proposed by Turnbull[12,13] in the intermediate temperature range.

There is some uncertainty for the binding energy of the Xe_{U_3O} cluster due to the challenges associated with DFT calculations of such a large cluster with high charge. For this reason we performed simulations with the vacancy binding energy set to -1.99 eV instead of -3.27 eV used in the simulations referenced above, which corresponds to ${}^oG^{UO_2}_{Xe_{U_3O}} = x - 3.81$ eV instead ${}^oG^{UO_2}_{Xe_{U_3O}} = x - 5.09$ eV. The results are also shown in Fig. 3b) and, as expected, the diffusivity lies in between the high and zero (zero gives the same result as for the model without the Xe_{U_3O} cluster) values for the binding energy. Additional

work should be performed to assess the best estimate of the Xe_{U_3O} cluster binding energy, since it has significant impact on the predicted effective Xe diffusivity.

B. Possible bubble contribution to irradiation enhanced diffusion at intermediate and low temperature

The various options for Xe diffusion under irradiation investigated in Fig. 3 all fail to capture the intermediate and low temperature irradiation enhanced diffusivity proposed by Turnbull[12,13] (this refers to the activated intermediate temperature diffusivity and not the athermal diffusion at the lowest temperatures). Based on the present results it is difficult to envision a vacancy or point defect mechanism that gives such a low activation energy and also very low pre-exponential factor. Diffusion of small fission gas bubbles is another mechanism that could be responsible for the irradiation enhanced diffusivity. However, this contribution is typically believed to be negligible in fission gas release models based on experimental measurements on irradiated fuel showing low mobility of bubbles[29,30]. Nevertheless, we investigate this possibility, simply because point defect mediated diffusion fails to capture this behavior and it is also possible that the in-pile conditions differ sufficiently from the out-of-pile experiments used to conclude that bubble diffusion is very slow. Bubble diffusion may be controlled by one of three mechanisms transferring atoms from one side of the bubble to the other: 1) volume diffusion of vacancies in the bulk around the bubble, 2) surface diffusion and 3) evaporation-condensation[29,31]. In the temperature and bubble size regime of interest to the present problem the surface diffusion mechanism should be most relevant. For surface diffusion controlled bubble migration the diffusivity is expressed as[29,31]:

$$D_b = \frac{3D_s\omega^{4/3}}{4\pi R_b^4}, \tag{27}$$

where D_s is the surface diffusivity, R_b the bubble radius and ω is the atomic volume of uranium atoms. We have calculated the activation energy for surface diffusion on the UO_2 (111) surface to be 1.26 eV. The pre-exponential factor is currently being calculated, but we assume that it is in the $10^{10}-10^{13}\mathrm{s}^{-1}$ range. If the attempt frequency is at the lower end, bubbles of radius $\sim 5-10$ nm are needed to reproduce the pre-exponential factor reported by Turnbull[12,13]. This is a rather large radius for fission gas bubbles in irradiated UO_2. However, there may also be other contributions to the pre-exponential factor that are not captured in this present model, i.e. the fraction of the total gas concentration captured in mobile bubbles. We have plotted the bubble diffusivity arising from the present model in Fig. 4. The pre-exponential factor was chosen to match the experimental model, which, even though the corresponding parameter values are reasonable, implies that the model is not a first principles prediction. The agreement with the experimental data is still encouraging and bubble diffusion mechanisms should be further investigated. However, at this point, the contribution from the bubble diffusion mechanism remains speculative. Also, if bubbles are mobile in irradiated UO_2 the rate theory model used to calculate the impact of trapping and resolution would have to be modified. These topics will be investigated in future work.

IV. BISON SIMULATIONS OF FISSION GAS RELEASE

We have implemented the Xe_{U_2O}, Xe_{U_3O} as well as the analytical model used in Ref. 21 in the BISON fuel performance code[32]. BISON incorporates a model for the analysis of fission gas release (FGR), which adopts and extends the treatment developed in Ref. 9. The first and basic step in FGR, namely, gas diffusion from within the fuel grains to the grain boundaries (intragranular diffusion), is computed through numerical solution of the relevant diffusion equation in spherical coordinates[2]. An effective fission gas diffusivity is employed that allows for the effects of intragranular bubbles, and is calculated based on the diffusivity of fission gas atoms[3,15]. For this purpose, the empirical correlation of Turnbull *et al.*[12,13] (see Section I) is used as standard option. In addition, the effective diffusivities calculated in this work, see Fig. 3, are incorporated in the code and considered in the present simulations. The diffusivities were implemented as piece-wise linear fits to the calculated curves in Fig. 3. In order to conform with the model by Turnbull[12], which used the diffusivity measured by Davies and Long[16] in H_2(g) atmosphere, we used the calculated diffusivity for the same conditions. Future work should consider the fuel chemistry in more detail.

Intragranular diffusion calculations are performed in BISON along with modeling of the subsequent stages of the FGR process. To this end, a direct description of the kinetics of gas bubbles at the grain boundaries is employed, which includes the fundamental mechanisms of bubble growth, coalescence, inter-connection and gas release after a grain boundary saturation condition is attained. Model details can be found in Ref. 33.

The BISON code incorporating the new fission gas diffusivities was applied to the simulation of a LWR fuel rod irradiation test from the International Fuel Performance Experiments database[34]. First the Risø-3 AN3 experiment[35] was considered, which comprises a base irradiation up to about 41 GWd/t in the BIBLIS A PWR (Germany) and a subsequent power ramp test in the DR3 research reactor at Risø (Denmark). This experiment was also selected in the framework of the IAEA coordinated research project on Fuel Modeling at Extended Burnup FUMEX-II[36]. Fig. 5 compares the calculated FGR during the ramp test with the available experimental data. The FGR is defined as the ratio between the amounts of fission gas released and generated

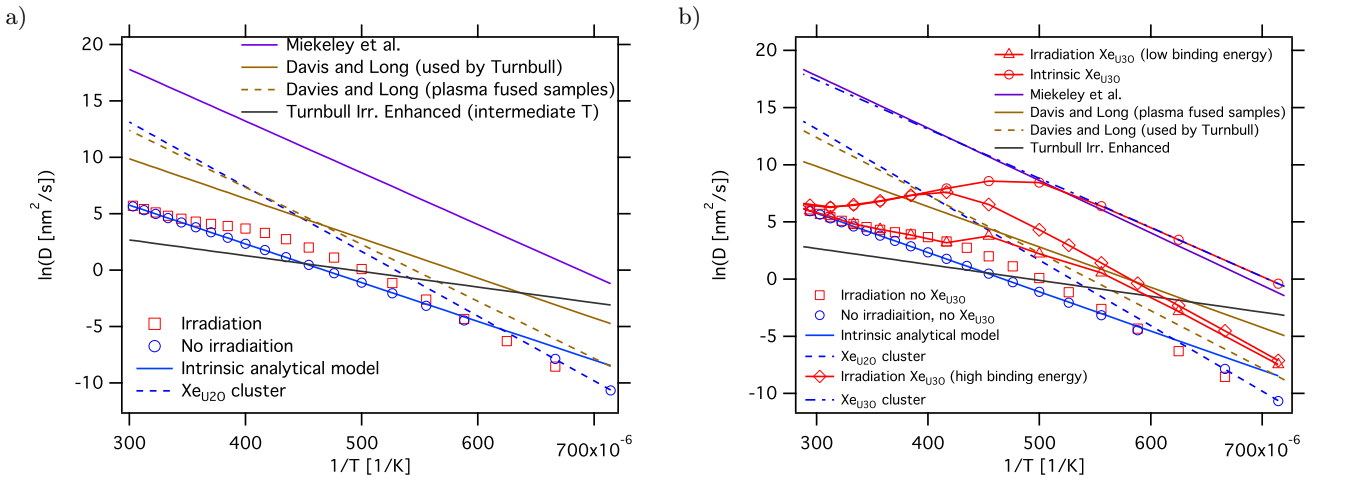

FIG. 3. a) The Xe diffusivity under irradiation conditions compared to the intrinsic diffusivity, the corresponding analytical expressions derived in Ref. 21 as well as the diffusivity of the Xe_{U_2O} cluster and the experimental data due to Miekelely *et al.*[18], Davies and Long[16] and Turnbull[12,13]. These results do not include the Xe_{U_3O} cluster. b) The same results as in a) but with the Xe_{U_3O} cluster included in the simulations. The diffusivities of the Xe_{U_2O} and Xe_{U_3O} clusters are also shown.

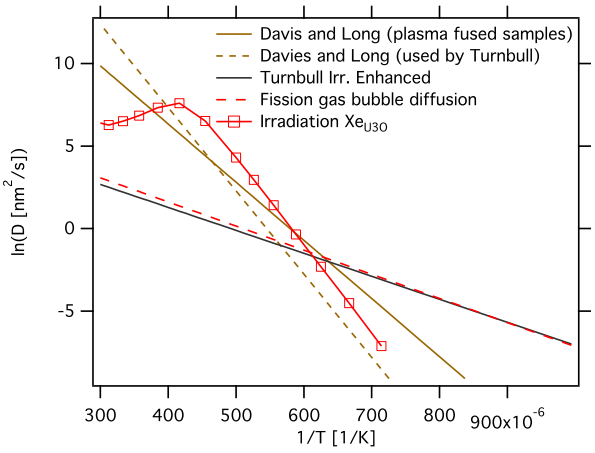

FIG. 4. The effective Xe diffusivity under irradiation conditions including the Xe_{U_3O} cluster compared to the experimental model proposed by Turnbull[12,13]. We also include the diffusivity for fission gas bubbles with surface diffusion as the rate-limiting step and the pre-exponential factor fitted to Turnbull's data[12,13], which is also consistent with diffusion models (see text).

in the fuel rod. Both on-line and post-irradiation FGR measurements are available and are shown in Fig. 5a). We also simulated another Risø power ramp experiment (Risø GE7). The FGR for this experiment is shown in Fig. 5b).

Incorporating the diffusivity of fission gas atoms in stoichiometric UO_2 calculated in this work in the BISON model leads to reasonable FGR predictions. Compared to the results obtained using the experimental model of Turnbull *et al.*[12,13]. For the Risø AN3 test the present model for the diffusivity leads to an improvement of the BISON predictions at the end of the base irradiation, while the prediction at the end of the ramp test exhibits slightly reduced accuracy. This is largely due to the much lower impact of irradiation at intermediate and low temperatures. The predicted FGR at the end of the ramp test is somewhat lower than experimental measurements and the prediction by the Turnbull model. The model that includes the Xe_{U_3O} cluster predicts higher release and it is in better agreement with experimental data. The high and low binding energies for this cluster gives almost identical results. The Risø GE7 test exhibits the same trends as for Risø-3 AN3 experiment. Again, the results between the low and high binding energies are almost indistinguishable. Compared to Turnull's model the FGR before the ramp test is underestimated, which is explained by the low diffusivity predicted by our models at intermediate and low temperatures. By including the diffusivity of fission gas bubbles (see Sec. III B) this discrepancy would be resolved. However, additional work is required before the best approach to model this contribution has been established.

These results demonstrate that it is possible to develop new and accurate material models from atomistic simulations for specific processes (intragranular fission gas diffusion) and then combine them with existing, partly empirical, models for the other FGR steps. However, additional validation work is still required to better assess the accuracy of the new fission gas diffusivity model. Particular attention should be devoted to mechanisms leading to irradiation enhanced diffusion in the intermediate and low temperature range.

V. CONCLUSIONS AND OUTLOOK

Continuum models for diffusion of xenon (Xe), uranium (U) vacancies and U interstitials in UO_2 were derived for both intrinsic conditions and under irradiation

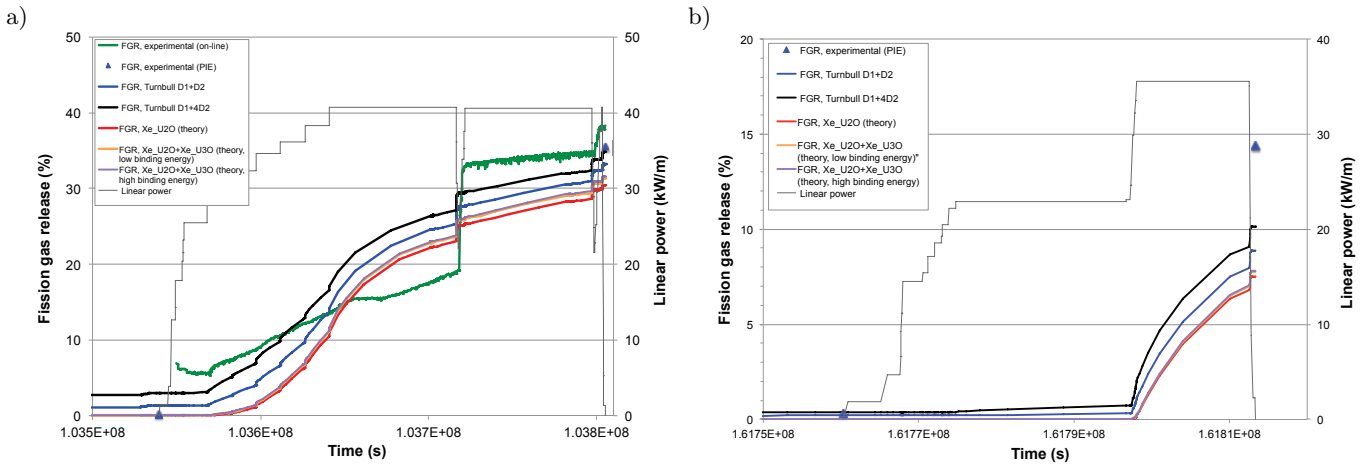

FIG. 5. a) BISON simulation of fission gas release for the Risø-3 AN3 experiment[35] using a number of different fission gas diffusion models. b) The same plot as in a), but for the Risø GE7 experiment.

by defining a set of reaction-diffusion equations. The mechanistic diffusion models were based on results from density functional theory (DFT) and empirical potential calculations[21], which were also used for determining the model parameters. Xe diffusion occurs by vacancy mechanisms. We include two mobile Xe clusters, Xe_{U_2O} (a Xe atom in a uranium + oxygen vacancy trap site with one bound uranium vacancy) and Xe_{U_3O} (a Xe atom in a uranium + oxygen vacancy trap site with two bound uranium vacancies). The high binding energy and mobility makes the Xe_{U_3O} cluster important, despite its large size decreasing the stability from an entropy perspective. If only the Xe_{U_2O} cluster is included in the simulations, radiation-enhanced diffusion occurs at intermediate temperature ($1785 < T < 2860$ K), while at low and high temperatures the diffusivity is given by the intrinsic values. At low temperature ($T < 1785$ K) cluster formation governs the diffusivity for both intrinsic and irradiation conditions. Both the intrinsic and the irradiation enhanced diffusivity is increased when the large Xe_{U_3O} cluster is considered. Even though this cluster only occurs in small concentrations, its high mobility leads to increased diffusivity for an extended temperature range. Interestingly, the Xe_{U_3O} cluster gives rise to effective Xe diffusivities that are higher for intrinsic conditions than under irradiation for a wide range of temperatures. Under irradiation the fast-moving Xe_{U_3O} cluster recombines quickly with irradiation induced interstitial U ions, while this mechanism is much less important for intrinsic conditions. The net result is higher concentration of the Xe_{U_3O} cluster for intrinsic conditions than under irradiation. This behavior finds support in experiments and can explain the surprisingly wide range of diffusivities reported in different experimental studies. However, all vacancy-mediated mechanisms underestimate the Xe diffusivity compared to the irradiation enhanced model proposed by Turnbull[12,13], which is used in most fission gas release simulations. We present tentative results suggesting that diffusion of small fission gas bubbles may give rise to the behavior reported by Turnbull[12,13], though this conclusion is still speculative.

The effective Xe diffusion models were implemented in the BISON fuel performance code and we simulated a few fission gas release tests, including the Risø-3 AN3 and GE7 experiments[35]. The new models predict lower fission gas release at the end of the base irradiation than present models (Turnbull), in good agreement with experiments for the Risø AN3 test but in slight disagreement with the Risø GE7 test. This is largely due to the much lower impact of irradiation enhanced diffusion at intermediate and low temperature in our model as compared to the Turnbull model. The predicted fission gas release at the end of the ramp test is lower than experimental measurements and the prediction by the Turnbull model for both the AN3 and GE7 tests. The model that includes the Xe_{U_3O} cluster predicts higher release and it is in better agreement with experimental data.

Future work will further explore the new Xe diffusion model, in particular the effect of various irradiation conditions (power history) on the effective Xe diffusivity and fission gas release as well as effects of chemistry. The possibility of fission gas bubbles contributing to the effective Xe diffusivity at intermediate and low temperature will be investigated, which involves revisiting the rate theory model used to describe trapping and resolution of fission gas by the small bubbles.

[1] D. R. Olander, Fundamental Aspects of Nuclear Reactor Fuel Elements, NTIS, ERDA, 1975.

[2] A. H. Booth, A method of calculating gas diffusion from UO_2 fuel and its application to the X-2-f test, Technical

Report Technical Report AECL 496 CRDC-721, Atomic Energy of Canada Limited, 1957.
[3] M. V. Speight, Nucl. Sci. Eng. 37 (1969) 180–185.
[4] K. Forsberg, A. R. Massih, J. Nucl. Mater. 135 (1985) 140–148.
[5] K. Forsberg, A. R. Massih, J. Nucl. Mater. 127 (1985) 141–145.
[6] K. Forsberg, A. R. Massih, Modelling Simul. Mater. Sci. Eng. 15 (2007) 335–353.
[7] D. D. Lanning, C. E. Beyer, C. L. Painter, FRAPCON-3: Modifications to Fuel Rod Material Properties and Performance Models for High-Burnup Application, Technical Report PNNL-11513-V1, Pacific Northwest National Laboratory, 1997.
[8] P. Lösönen, J. Nucl. Mater. 280 (2000) 56–72.
[9] G. Pastore, L. Luzzi, V. Di Marcello, P. Van Uffelen, Nucl. Eng. Des. 256 (2013) 75–86.
[10] J. A. Turnbull, J. Nucl. Mater. 50 (1974) 62–68.
[11] J. A. Turnbull, C. A. Friskney, J. Nucl. Mater. 71 (1978) 238–248.
[12] J. A. Turnbull, C. A. Friskney, J. R. Findlay, F. A. Johnson, A. J. Walter, J. Nucl. Mater. 107 (1982) 168–184.
[13] J. A. Turnbull, R. J. White, C. Wise, in: Proceedings of Technical Committee Meeting on Water Reactor Fuel Element Computer Modelling in Steady State, Transient and Accident Conditions, Preston, UK, Sept. 18-22, pp. 174–181.
[14] H. J. Matzke, J. Chem. Soc. Faraday Trans. 2 83 (1987) 1121–1142.
[15] R. J. White, M. O. Tucker, J. Nucl. Mater. 118 (1983) 1–38.
[16] D. Davies, G. Long, The emission of xenon-133 from lightly irradiated uranium dioxide spheroids and powders, Technical Report AERE Rep. No. 4347, Atomic Energy Research Establishment, Harwell, 1963.
[17] G. T. Lawrence, J. Nucl. Mater. 71 (1978) 195–218.
[18] W. Miekeley, F. W. Felix, J. Nucl. Mater. 42 (1972) 297–306.
[19] R. M. Cornell, Phil. Mag. 19 (1969) 539–554.
[20] K. N. G. Kaimal, M. C. Naik, A. R. Paul, J. Nucl. Mater. 168 (1989) 188–190.
[21] D. Andersson, P. Garcia, X.-Y. Liu, G. Pastore, M. Tonks, P. Millett, B. Dorado, D. Gaston, D. Andrs, R. Williamson, R. Martineau, B. Uberuaga, C. Stanek, Journal of Nuclear Materials 451 (2014) 225–242.
[22] C. R. A. Catlow, Proc. R. Soc. Lond. A 364 (1978) 473–497.
[23] R. G. J. Ball, R. W. Grimes, J. Chem. Soc., Faraday Trans. 86 (1990) 1257–1261.
[24] D. A. Andersson, B. P. Uberuaga, P. V. Nerikar, C. Unal, C. R. Stanek, Phys. Rev. B 84 (2011) 054105.
[25] M. R. Tonks, D. Gaston, P. C. Millett, D. Andrs, P. Talbot, Comput. Mater. Sci. 51 (2012) 20.
[26] D. Gaston, G. Hansen, S. Kadioglu, D. Knoll, C. Newman, H. Park, C. Permann, W. Taitano, J. Phys.: Conf. Ser. 180 (2009) 012012.
[27] M. Tonks, D. Gaston, C. Permann, P. Millett, G. Hansen, D. Wolf, Nucl. Eng. Design 83 (2010) 2877.
[28] J. R. MacEwan, W. H. Stevens, J. Nucl. Mater. 11 (1964) 77–93.
[29] J. A. Turnbull, J. Nucl. Mater. 62 (1976) 325–328.
[30] C. Baker, J. Nucl. Mater. 66 (1977) 283–291.
[31] M. S. Veshchunov, V. E. Shestak, J. Nucl. Mater. 376 (2008) 174–180.
[32] R. L. Williamson, J. D. Hales, S. R. Novascone, M. R. Tonks, D. R. Gaston, C. J. Permann, D. Andrs, R. C. Martineau, J. Nucl. Mater. 423 (2012) 149–163.
[33] G. Pastore, J. D. Hales, S. R. Novascone, D. M. Perez, B. W. Spencer, R. L. Williamson, in: LWR Fuel Performance Meeting – TopFuel 2013, Charlotte, NC, USA, September 15–19.
[34] E. Sartori, J. Killeen, J. A. Turnbull, International fuel performance experiments (IFPE) database, 2010.
[35] The Third Risø Fission Gas Project, BUMP TEST AN3 (CB8-2R), Technical Report RISØ-FGP3-AN3, 1990.
[36] Fuel Modelling at Extended Burnup (FUMEX-II), Technical Report Technical Report IAEA-TECDOC-1687, IAEA, IAEA, 2012.